JOURNAL OF AIRCRAFT
Vol. 31, No. 2, March–April 1994

Computational Analysis of Off-Design Waveriders

X. He* and M. L. Rasmussen†
University of Oklahoma, Norman, Oklahoma 73019

Comprehensive inviscid and viscous numerical simulations of hypersonic flow past nonconical rounded-nose waveriders are presented. The flowfields and aerodynamic forces at off-design conditions are determined inviscidly by a space marching CFD code with the initial data plane provided by a time marching Navier-Stokes CFD code. Off-design conditions include off-design Mach numbers, angles of attack, and rounded leading edges. A wide range of waverider configurations is investigated and compared. On-design viscous flows past a waverider with a sharp leading edge at $M_\infty = 4$ and at different Reynolds numbers and temperature boundary conditions are obtained by a time marching Navier-Stokes solver. These calculations show the effects of viscous interactions, which are influential near the leading edges, and determine the viscous drag. The inviscid calculations show that L/D decreases as M_∞ increases (with $\alpha = 0$). At the on-design Mach numbers, the maximum L/D may occur at slight positive or negative α, depending on the shape of the waverider, and zero lift occurs at a negative α approximately equal to half of the body thickness. The effects of slight leading-edge blunting produce only local effects in the flowfield and small losses in L/D. The characters of the flowfields in the base plane are illustrated.

Introduction

THE concept of waveriders as a means for designing aerodynamic lifting-body configurations has been around for some time. The first waveriders stemmed from the two-dimensional-flow caret configurations of Nonweiler[1] which amounted to a type of delta wing. The natural extension of this was to waveriders derived from axisymmetric cone flows, first studied by Jones.[2] This was extended further to nonaxisymmetric cone flows by Rasmussen.[3] Of course, waveriders can be derived from many different kinds of known supersonic inviscid flowfields. The known high-pressure streamlines behind a known oblique shock surface imbedded in a uniform freestream flow are taken to form a compression undersurface for some new body, and then the upper surface is usually formed by a continuation of the freestream itself. The freestream surface, the new compression surface, and the oblique shock surface all intersect along some curve that forms a sharp leading edge for some newly constructed body. Because the shock extends only underneath the body constructed in such a way, the body is called a waverider. There are variations on this scheme, but the waveriders so constructed are said to be at the on-design conditions, and the flowfields and aerodynamic forces and moments are known for these conditions.

Since the aerodynamic properties of on-design waveriders are known, they can be very useful for determining some features of lifting bodies in general, especially with regards to optimization. For the case of inviscid flows, pertinent studies were made by Cole and Zien[4] and Kim et al.[5] by means of the calculus of variations. When viscous effects were taken into account by boundary-layer theory, Bowcutt et al.[6] developed a numerical scheme for obtaining viscous optimized waveriders. These studies were concerned with maximizing L/D subject to suitable constraints. In the design of hypersonic vehicles, however, there may be numerous factors (or constraints) that influence a configuration and which thus mitigate settling on any single optimized shape. Such factors may be volumetric packaging, stability and control surfaces, air-breathing propulsion units, and landing and takeoff considerations. Therefore, it may be that a broader view of the factors that affect the shaping of a waverider may be of interest; a study directed towards this end was made by Rasmussen and He.[7]

When the shape of a waverider is fixed and the flow conditions deviate from the specified on-design conditions, the waverider is said to be at off-design conditions. This generally occurs when the freestream flow is at a different Mach number and/or when the waverider is misaligned with the freestream flow. When the Mach number is sufficiently high, moreover, it may be that the sharp leading edges should be rounded to reduce the catastrophic effects of aerodynamic heating. When the leading edges are rounded, or for that matter, when the shape is altered, the altered waverider can also be said to be at off-design conditions. Contrary to the case for on-design conditions, the aerodynamic properties of waveriders at off-design conditions cannot be obtained by any simple analysis, and resort must be made to elaborate numerical computational methods.

Some of the first computational analyses were directed to a class of elliptic-cone derived waveriders for which both the waverider and its inviscid flow were conical (but not axisymmetric), and for which experimental results are available.[8,9] Potential-flow analyses were made by Jones and coworkers.[10–12] Long[13] used an Euler CFD code to consider the elliptic-cone derived waverider as well as an altered variation. Liao et al.[14] utilized a Navier-Stokes code so that viscous effects could be taken into account. Yoon[15] used an Euler code to study several elliptic-cone derived waveriders under a wide range of off-design conditions.

Computation analyses have also been made for waveriders derived from axisymmetric conical flows. For these waveriders, the inviscid flowfields are conical, but the waverider bodies themselves are not. The first calculations were made by Jones and Dougherty[16] using an Euler code and later by Jones et al.[17] using a Navier-Stokes code. These results were directed toward validating two so-called viscous-optimized waveriders designed by the Bowcutt-Anderson method and for which experimental results were available.

For waveriders derived from axisymmetric conical flows, a very large variety of shapes can be obtained, and a study of the aerodynamics for a variety of these shapes at off-design conditions is the subject of this article. Besides the lift and drag as a function of angle of attack, the nature of the flowfield

Received Dec. 14, 1992; revision received Feb. 8, 1993; accepted for publication Feb. 8, 1993.

*Adjunct Assistant Professor, School of Aerospace and Mechanical Engineering, 865 Asp Ave. Member AIAA.

†Professor, School of Aerospace and Mechanical Engineering, 865 Asp Ave. Associate Fellow AIAA.

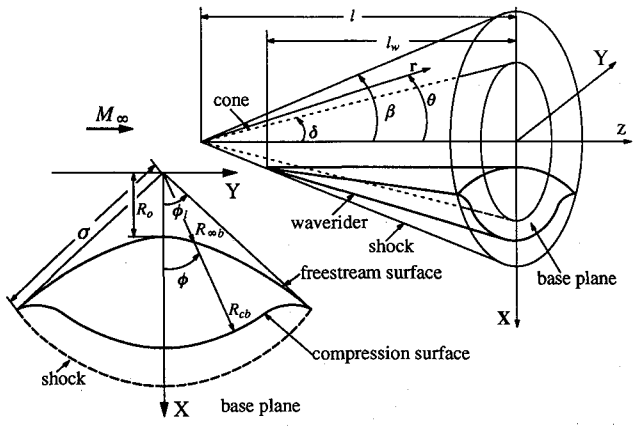

Fig. 1 Construction of a general cone-derived waverider.

is also of interest when the Mach number is both above and below the design value and for both positive and negative angles of attack. Waverider shapes for the design Mach numbers of 4 and 8 are considered, and the effects of rounding of the leading edge for the $M_\infty = 8$ waveriders are investigated. Most of the calculations are performed with an Euler code, but a few calculations are performed with a Navier-Stokes code to ascertain the effects of viscous interactions. The investigation is meant to be comprehensive and to establish some of the main features of waverider aerodynamics.

Formulation

Consider steady inviscid supersonic flow of a perfect gas past a circular cone at zero incidence with the freestream and at Mach number M_∞. The coordinate system and nomenclature are shown in Fig. 1. The waverider and its on-design flowfield are to be described by means of hypersonic small disturbance theory (HSDT) following the methodology of Rasmussen and He.[7] The shock angle β is related to the basic-cone angle δ by means of the relation

$$\sigma \equiv \frac{\beta}{\delta} = \left[\frac{\gamma + 1}{2} + \frac{1}{K_\delta^2}\right]^{1/2} \tag{1}$$

where $K_\delta \equiv M_\infty \delta$ is the hypersonic similarity parameter. In spherical polar coordinates (r, θ, ϕ), the freestream surface is described by

$$r = (\beta/\theta) r_s(\phi) \tag{2}$$

where $r = r_s(\phi)$ is the leading-edge line drawn on the conical shock $\theta = \beta$. The compression surface in the shock layer is described by

$$r = r_s(\phi)\sqrt{\frac{\beta^2 - \delta^2}{\theta^2 - \delta^2}} \tag{3}$$

The freestream surface and the compression surface can thus be determined when $r_s(\phi)$ is known.

There are various equivalent ways in which the function $r_s(\phi)$ can be specified. One way is by the direct specification of a line along the shock surface. Another might be the specification of the projected planform surface. The method utilized here is the specification of the trailing-edge of the freestream surface in the base plane. This is done by setting $\theta = \theta_{\infty b}(\phi)$ when $r = l$ in Eq. (2), where l is the length of the basic cone:

$$\theta_{\infty b}(\phi) = \beta[r_s(\phi)/l] \tag{4a}$$

The ratio $R_{\infty b} \equiv \theta_{\infty b}/\delta$ is now introduced as the normalized radial distance from the basic-cone axis to a point on the freestream surface, i.e.

$$R_{\infty b}(\phi) = \sigma[r_s(\phi)/l] \tag{4b}$$

as shown in Fig. 1. Thus $R_{\infty b} = 1$ at the surface of the basic cone, and $R_{\infty b} = \sigma$ at the shock where $\phi = \phi_l$.

Although $R_{\infty b}(\phi)$ could be specified by cylindrical coordinates, it is convenient alternatively to work in rectangular Cartesian coordinates in the base plane. To this end, the normalized coordinates $X \equiv x/(l\delta)$ and $Y \equiv y/(l\delta)$ are introduced, such that

$$\begin{aligned} X &\equiv R_{\infty b}\cos(\phi) \\ Y &\equiv R_{\infty b}\sin(\phi) \\ R_{\infty b} &\equiv (X^2 + Y^2)^{1/2} \end{aligned} \tag{5}$$

The freestream surface, trailing-edge curve can be established by specifying X as a function of Y. The class of shapes generated by the even quartic polynomial

$$X = R_0 + AY^2 + BY^4 \tag{6}$$

are considered here, where R_0, A, and B are constants that remain to be specified. By means of this method, $R_{\infty b}$ is specified as a function of Y instead of ϕ, and correspondingly from Eq. (4b), so is the function r_s. The constants R_0, A, and B cannot all be specified independently. At the intersection of the freestream and compression surfaces on the shock, we must have $R_{\infty b} = \sigma$ at $\phi = \phi_l$ such that $X = X_\sigma \equiv \sigma\cos\phi_l$ and $Y = Y_\sigma \equiv \sigma\sin\phi_l$. Thus, from Eq. (6), only two of the constants R_0, A, and B can be specified independently.

The parameter R_0 can be interpreted geometrically as the distance down to the freestream surface from the basic-cone axis, measured in the plane of symmetry, i.e., when $\phi = 0$ (Fig. 1). It can also be used to determine the length l_w of the waverider, i.e.

$$(l_w/l) = 1 - (R_0/\sigma) \tag{7}$$

It is useful to determine the remaining parameters in terms of the slope m_∞ of the freestream surface trailing edge at the shock

$$m_\infty \equiv \tan\Omega_\infty \equiv \left(\frac{dX}{dY}\right)_\sigma = 2AY_\sigma + 4BY_\sigma^3 \tag{8}$$

Thus, A and B can be evaluated in terms of X_σ, Y_σ, R_0, and m_∞

$$\begin{aligned} A &= \frac{4(X_\sigma - R_0) - m_\infty Y_\sigma}{2Y_\sigma^2} \\ B &= \frac{-2(X_\sigma - R_0) + m_\infty Y_\sigma}{2Y_\sigma^4} \end{aligned} \tag{9}$$

Illustrative Waverider Shapes

To show how different configurations behave under off-design conditions, five different shapes having an on-design Mach number of $M_\infty = 4$ are selected. They are labeled C1 to C5, and their base-plane shapes are shown in Fig. 2. They are scaled to have the same length l_w. A perspective view for C5 is shown in Fig. 3. The geometric and aerodynamic properties are calculated by HSDT[7] and are listed in Table 1. The forebody viscous drag is determined according to a laminar boundary layer with a freestream Reynolds number, based on the waverider length, of 7.7×10^7. The base drag is arbitrarily set to zero, i.e., $p_b = p_\infty$. The angle between the

Table 1 Properties of illustrative waveriders

Configurations	C1	C2	C3	C4	C5	C6	C7	C8
M_∞	4	4	4	4	4	8	8	8
δ	8	10	10	15	10	10	10	10
R_0/X_σ	0.35	0.7	0.6	0.5	0.4	0.44	0.4	0.7
Ω_∞	28.6 deg	0	−16.7 deg	0	14.2 deg	30.0 deg	21.8 deg	21.8 deg
ϕ_l	50 deg	50 deg	70 deg	50 deg	50 deg	27.2 deg	50 deg	50 deg
Λ_b	3.2 deg	10.5 deg	10.4 deg	17.9 deg	9.1 deg	24.3 deg	20.1 deg	20.1 deg
b/l_w	0.579	0.877	0.744	0.859	0.649	0.344	0.471	0.636
S_w/S_p	2.177	2.039	2.050	2.108	2.287	2.494	2.143	2.047
$V^{2/3}/S_p$	0.132	0.145	0.163	0.222	0.161	0.239	0.223	0.199
$Re_{lw} \times 10^{-7}$	7.7	7.7	7.7	7.7	7.7	15.4	15.4	15.4
$C_L \times 10$	0.506	0.712	0.759	1.566	0.745	0.668	0.679	0.663
$C_f \times 10^3$	0.210	0.215	0.221	0.245	0.225	0.137	0.196	0.192
$C_D \times 10^2$	0.443	0.809	0.971	3.189	0.854	0.955	1.058	1.019
L/D	11.43	8.804	7.821	4.912	8.716	6.997	6.415	6.512
$(L/D)_{\text{inviscid}}$	12.75	9.308	8.204	4.993	9.276	7.255	6.680	6.773

C_f = Average skin-friction coefficient.[7]

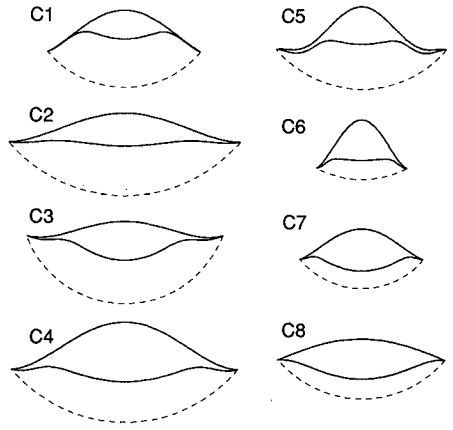

Fig. 2 Base-plane views of illustrative waveriders.

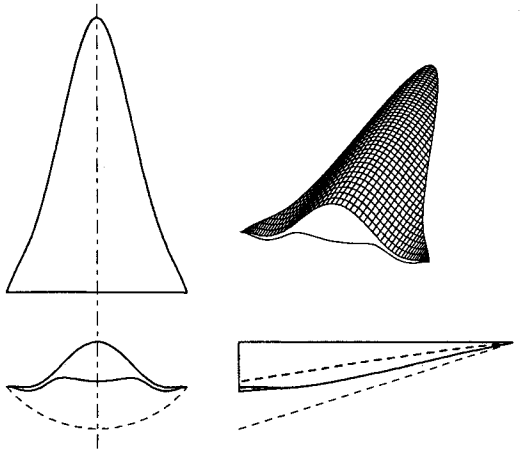

Fig. 3 Perspective views of configuration C5.

freestream and compression surfaces where they intersect in the base plane is denoted by Λ_b, and the ratio of base width to length is denoted by b/l_w. The volume, projected planform area, and forebody wetted-surface area are denoted by V, S_p, and S_w. The lift and drag coefficients are based on S_p. The waveriders denoted by C1 to C4 are based on Eq. (6), but the configuration C5 is based on an even sixth-order polynomial that produces a reflexed trailing edge.[7,18]

Three different shapes—C6 through C8—with an on-design Mach number of $M_\infty = 8$ have also been selected, based on Eq. (6). Their on-design characteristics are also listed in Table 1, and the base-plane shapes are shown in Fig. 2. The leading-edge tips of waverider C6 will be rounded by means of a smooth curve produced by a third-order continuous B-spline. The modified configuration has a smaller span than

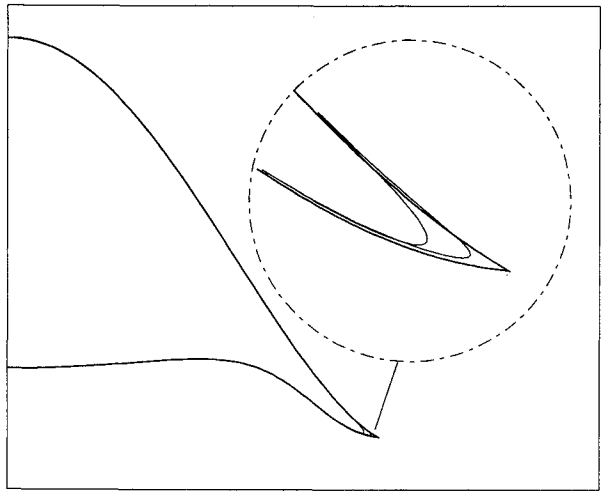

Fig. 4 Base-plane views of configuration C6 with and without rounding at the leading edge.

the on-design configurations. In this study, two cases of different rounding are used. The waveriders with sharp leading edges are first rounded to 98% of the span. To keep the curvature of rounding nearly a constant along the leading edge, the modified shape has a span of 98% of the original span in the base plane and about 94% near the nose. The second rounding procedure has a more blunt edge, which measures 96% of span in the base plane and about 92% near the nose. Figure 4 shows the base-plane view of C6. The dark line describes the on-design configuration and the light line describes the different amount of rounding.

Numerics

For a comprehensive investigation of off-design performances, considerable CPU time is required if an unsteady time marching code is used. The computational dimension, however, can be reduced by one if a space marching scheme is adopted to calculate the steady-state solution. The difficulty involved in adopting a space marching scheme for a nonconical waverider is that it requires an initial data plane to start the calculation. This initial data plane does not exist at off-design conditions. An unsteady time marching code CFL3D developed by Thomas and Walters[19] is therefore used to calculate the inviscid flowfield (by turning off the viscous terms) for the first 1% of the upstream body. The data calculated at the 1% cross section can therefore be used as the initial data plane, and a steady-state space marching code STARS3D developed by Lawrence et al.[20] is then used similarly for the calculation of the inviscid flowfield around the rest of the body. The use of a space marching scheme greatly reduces the CPU time and makes it possible to carry out the inves-

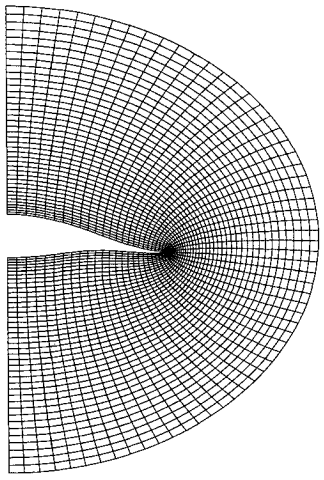

Fig. 5 Inviscid computational grid for a Mach 4 waverider.

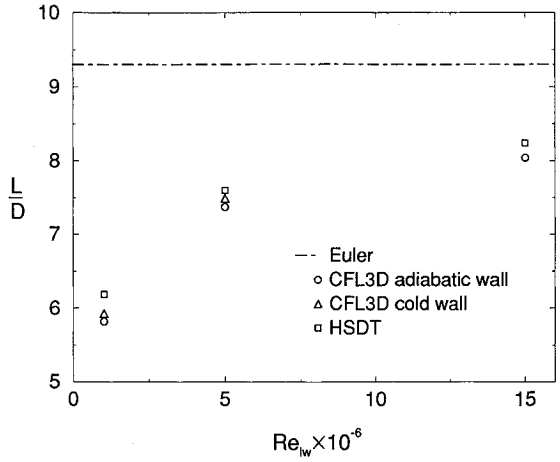

Fig. 6 *L/D* for Euler and Navier-Stokes calculations.

tigation on SPARC workstations. The viscous calculations by the space marching code, however, were not successful since a large pressure gradient caused eigenvalues to go negative and resulted in divergence. They were performed on an IBM 3090 supercomputer using the time marching CFL3D code.

The time marching code uses an implicit, finite-volume, upwind algorithm, and the governing equations are solved in conservation law form under a generalized coordinate transformation. Second-order central differencing is used for the viscous fluxes, and the thin-layer approximation is made for each direction. The approximate Riemann's solver of Roe[21] is used for the numerical inviscid fluxes with a third-order discretization. The spatially split approximate factorization method is used for time integration. The convective and pressure terms in each of the spatial factors are treated with first-order accurate upwind differences. The algorithm used in the space marching code is also based on Roe's scheme, but is modified in order to make it suitable for application to space marching calculations. It is implicit, uses finite volumes, and is second-order accurate in the crossflow directions.

The technique used for grid generation was developed by Thompson.[22] Control of the spacing of the grid lines on the body, symmetry plane, and freestream boundary was accomplished artificially by means of a stretching function.[18] The grid lines inside the region were spaced according to the source terms during convergence, and the grid points on the symmetry plane need to be redistributed accordingly. The redistribution of the grid points on the symmetry plane is updated every iteration by the intersection of the inner grid lines and the symmetry plane. The freestream boundary is given by an adjustable ellipse. The distribution of grid points on the waverider wall is controlled in such a way that the change of the size of the two adjacent grid spaces relative to the adjacent grid spacing is less than 30%.

The result of a typical grid generation is shown in Fig. 5. For the space marching calculations, the grid generated in a previous step is adjusted by the boundary movement and then used as initial values for the next step. A successive over-relaxation technique is used to accelerate the convergence with a calculated optimum acceleration parameter. The grid for the inviscid calculations with the space marching scheme is 61 × 41. The grid for the viscous calculations with the time marching scheme is 61 × 49 × 62. The grid for a waverider with a rounded edge is 67 × 41. Increasing the grid to 71 × 51 for an inviscid calculation involves considerable more computing effort, but without noticeable improvement in accuracy.

Viscous Results

Only a few laminar flow Navier-Stokes calculations are discussed here so that the ensuing inviscid results can be interpreted accordingly. Among the eight sample waveriders, C2 is chosen for the viscous computation since its aerodynamic and geometric features are moderate. At the on-design condition, the shock wave detaches from the leading edge owing to the boundary-layer displacement effects. Near the leading edges, viscous-interaction effects are of concern (as well as heat transfer which is not discussed here). To limit the use of the time-consuming unsteady scheme, the Navier-Stokes calculations are done only at the on-design condition. The Reynolds number is varied and different temperature boundary conditions are imposed to study the effects of viscous interaction. The Reynolds number is chosen to be 10^6, 5×10^6, and 1.5×10^7. These Reynolds number changes can be viewed as being caused by a change in flight altitude and/or a change in body length. An adiabatic wall and a moderately cold wall of $T_w/T_\infty = 2$ are used as temperature boundary conditions.

Figure 6 shows *L/D* at the on-design Mach number 4 and zero angle of attack for different Reynolds numbers and temperature boundary conditions. The *L/D* calculated by CFL3D is little lower than that for HSDT. The possible reasons for the discrepancy may include 1) the linear power law for the viscosity-temperature relation for HSDT tends to make C_D too big; 2) the higher pressure on the freestream surface due to viscous interaction tends to make C_L smaller for the Navier-Stokes results; and 3) the assumption of local flat-plate friction for both freestream and compression surfaces in HSDT introduces error. Reason 1 causes *L/D* for HSDT to be lower than it should, and reason 2 causes *L/D* for the Navier-Stokes calculations to be lower. Apparently, reasons 2 and 3 prevail, and *L/D* for the numerical calculations is somewhat smaller than that of HSDT. The *L/D* with a cold wall is slightly higher than with an adiabatic wall. At a lower temperature, the viscosity is smaller and so are the viscous effects.

The pressure profiles for configuration C2 for $Re_{lw} = 10^6$ and adiabatic walls are shown in Fig. 7 for the base plane. The viscous effects tend to make the shock stand off a little, and a compression disturbance occurs on the upper surface. The pressure distribution at the wall in the base plane is shown in Fig. 8. The solid line indicates the Euler solution. For the viscous results, a marked increase in pressure occurs at the leading edge on both the compression side and the freestream side. The maximum value for this jump increases as Re_{lw} decreases. Immediately downstream of the leading edge, the flow rapidly expands and then compresses to a pressure slightly higher than the inviscid value. As Re_{lw} decreases, the pressure increases considerably near the edge, and less so for the rest of the freestream surface. The increase in pressure at the edge on both sides of the waverider arises because of viscous interaction.

Figure 9 shows the pressure distributions in the stream direction very near the symmetry plane on the freestream surface. Without any viscous effects, the normalized pressure on

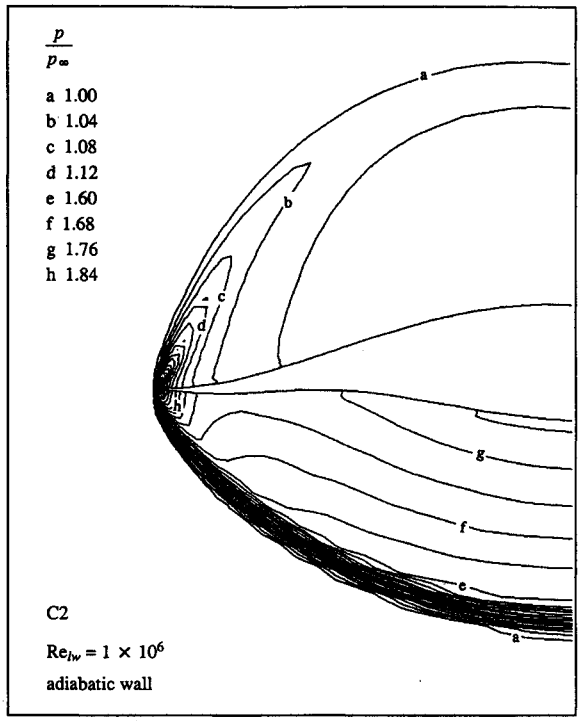

Fig. 7 Pressure contours for an adiabatic wall and $Re_{l_w} = 10^6$.

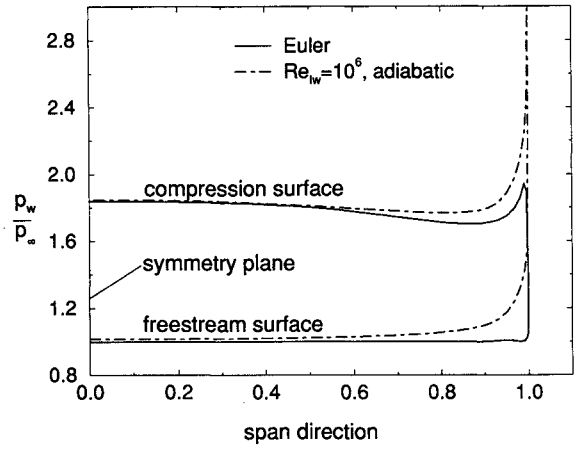

Fig. 8 Comparison of Euler and CFL3D results for surface pressure in base plane at $M_\infty = 4.0$ and $\alpha = 0$.

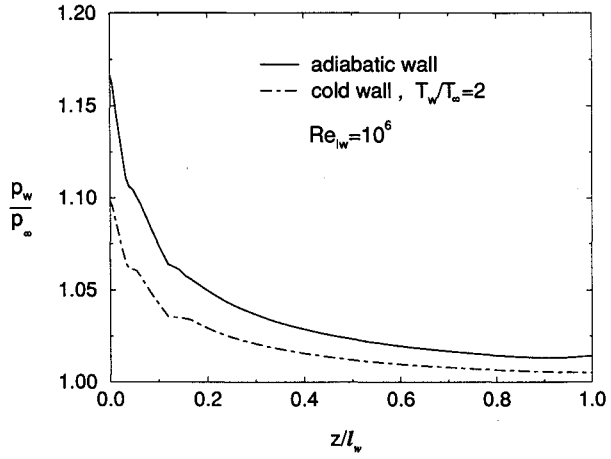

Fig. 9 Pressure in z direction in the symmetry plane on the freestream surface.

the upper surface is unity. With viscous interaction, the pressure ratio p/p_∞ is higher near the leading edge and close to unity for the rest of the body. The pressure for an adiabatic wall is higher than that for a cold wall since stronger viscous effects occur at a higher temperature. For the compression surface[18] the pressure is higher at the leading edge owing to viscous interaction. It decreases rapidly to adjust itself to the inviscid results which increase slowly along the conical-flow streamline. The higher pressure during the first 20% of the forebody is due to viscous interaction. The viscous results obtained for the cold-wall temperature boundary condition are closer to the Euler results. Further calculations, including temperature distributions, can be found in Ref. 18.

Inviscid Results for $M_\infty = 4$

The inviscid results are calculated by the space marching scheme starting from an initial data plane slightly downstream of the nose leading edge. The initial data plane was provided by the time marching scheme, and for the on-design conditions also by the HSDT solution. For the on-design conditions, a comparison of the results obtained by the two means for obtaining the initial data plane provided a measure of the validity of the inviscid Euler calculations. The small deviations from the two types of initial data planes vanished as the numerical scheme marched to the base plane, where the two results ended in very good agreement.[18] It was found, however, that the shock was slightly detached from the leading edge at $M_\infty = 4$ and $\alpha = 0$, which was the on-design condition. As was determined by Yoon,[15] this occurs because, besides the numerical error, the body shape is also slightly in error because it was based on the HSDT approximation. When M_∞ was increased to 4.2, the shock became attached to the leading edge, and the disturbance on the upper freestream surface disappeared. The on-design Mach number was thus regarded as $M_\infty = 4.2$.

Figure 10 shows configuration C2 at the inviscid on-design condition $M_\infty = 4.2$ and $\alpha = 0$, which is to be compared with the corresponding viscous result shown in Fig. 7. The flow in the shock layer is very uniform and conical. Corresponding results are found also for all the other configurations at the on-design conditions.

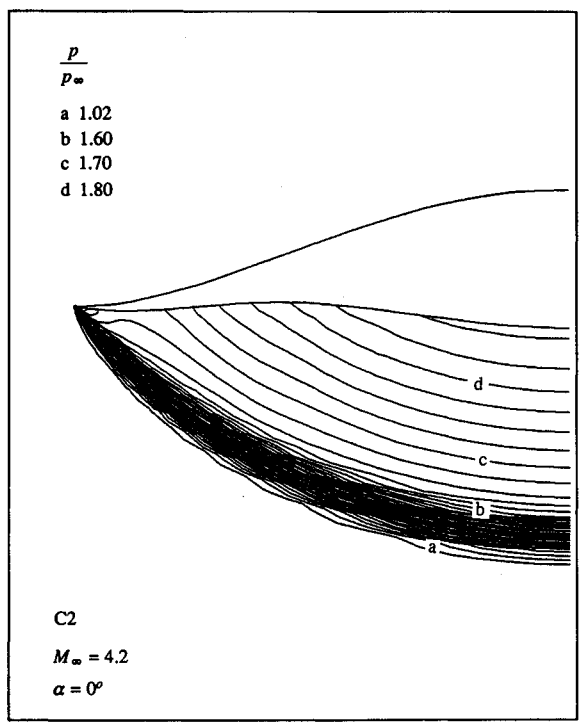

Fig. 10 Pressure contours in the base plane at Mach 4.2 and $\alpha = 0$ for C2.

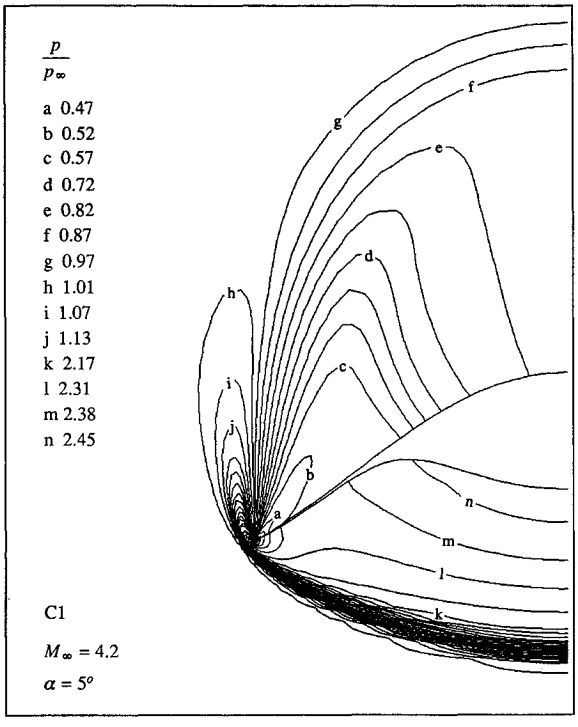

Fig. 11a Pressure contours in the base plane at Mach 4.2 and α = 5 deg for C1.

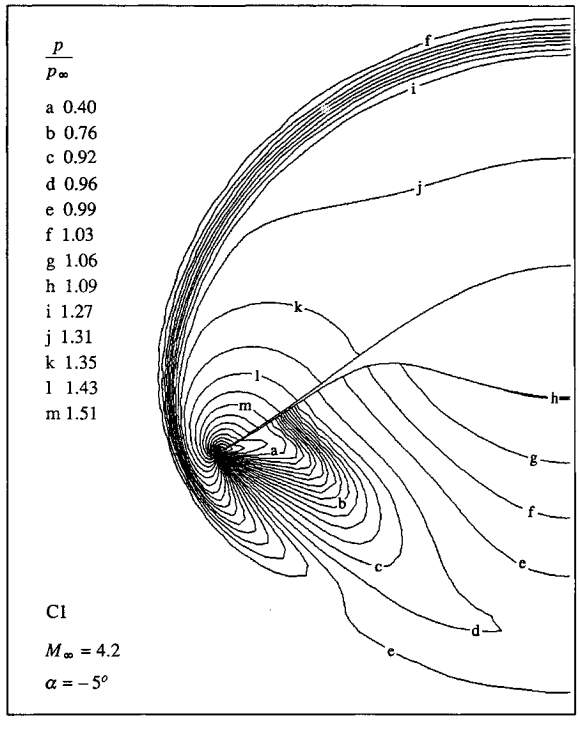

Fig. 11b Pressure contours in the base plane at Mach 4.2 and α = −5 deg for C1.

Figures 11a and 11b show the pressure contours in the base plane for configuration C1 at M_∞ = 4.2 and α = 5 and −5 deg. This configuration represents the extreme with its very thin winglets. At the on-design condition, the shock is attached and the flow in the shock layer is simple and conical and very analogous to that for configuration C2 shown in Fig. 9. For α = 5 deg (Fig. 10a), the shock is detached and there are expansion disturbances above the freestream surface. At α = −5 deg (Fig. 10b), the shock is detached and lies above the freestream surface; the flow expands about the leading edge and then recompresses on the lower surface. The lift has nearly decreased to zero at α = −5 deg.

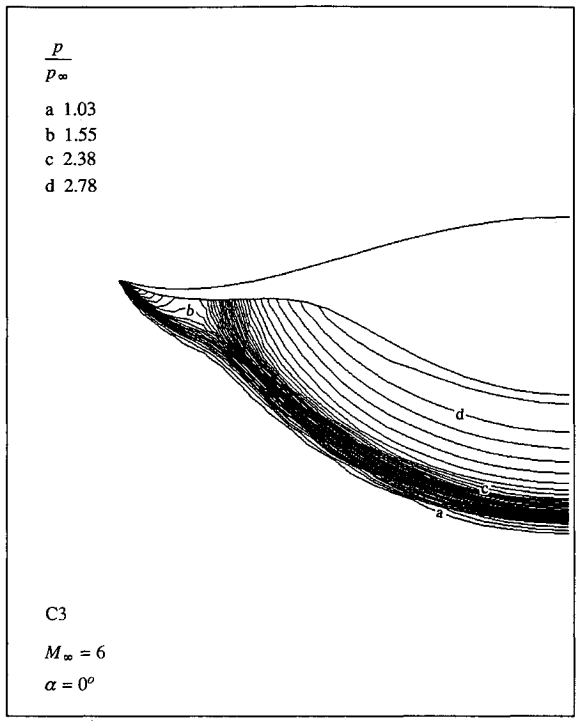

Fig. 12 Pressure contours in the base plane at Mach 6 and α = 0 for C3.

Figure 12 shows the pressure contours in the base plane for configuration C3 at α = 0, and the upper off-design Mach number M_∞ = 6. For this case the shock is attached and the flow disturbances confined to the shock layer underneath the body. Near the center plane of the body the flow is nearly conical, but outboard near the winglets a lambda-type shock appears to have formed. Similar results are obtained also for configurations C4 and C5.[18] This type of behavior for Mach numbers above the design Mach number was also discovered by Yoon[15] for elliptic cone waveriders.

Figures 13a and 13b pertain to two off-design conditions for configuration C5 which represents those type of configurations with reflexed trailing edges. Figure 13a shows pressure contours in the base plane for M_∞ = 4.2 and α = −5 deg. The main bow shock is detached and lies above the upper freestream surface. The flow continues to compress towards the upper surface and coalesces into a strong shock above the leading-edge tip. The flow expands around the tip, where it shows a pronounced vortical behavior and then compresses along the surface toward the symmetry plane. At α = 0 and the lower off-design Mach number M_∞ = 3 shown in Fig. 13b, the shock is detached but lies mostly underneath the body. There is an expansion of the flow around the tip towards the upper side. Note that viscous effects also cause the shock to detach, but for the viscous case compression disturbances develop on the upper surface near the leading edge.

The inviscid lift-to-drag ratio for these configurations is shown as a function of M_∞ (with α = 0) in Fig. 14. The values for M_∞ = 2, 3, 4, 6, and 8 were obtained numerically and then the curves produced by a spline fit. For an idealized waverider,[5,7] L/D is approximately inversely proportional to δ when $K_\delta \equiv M_\infty \delta$ is large. This is approximately true also for the waveriders studied here. The curves show the same off-design trends for all the waveriders. Both C_L and C_D decrease as M_∞ increases,[18] and so does their ratio, as shown in Fig. 14. The very thin extended winglets for configuration C1 produce a stronger variation of L/D with M_∞. Configurations C2 and C5 both were developed for M_∞ = 4, δ = 10 deg, and ϕ_l = 50 deg, and have nearly the same value of L/D at the on-design condition, but the dramatic reflexed trailing edge

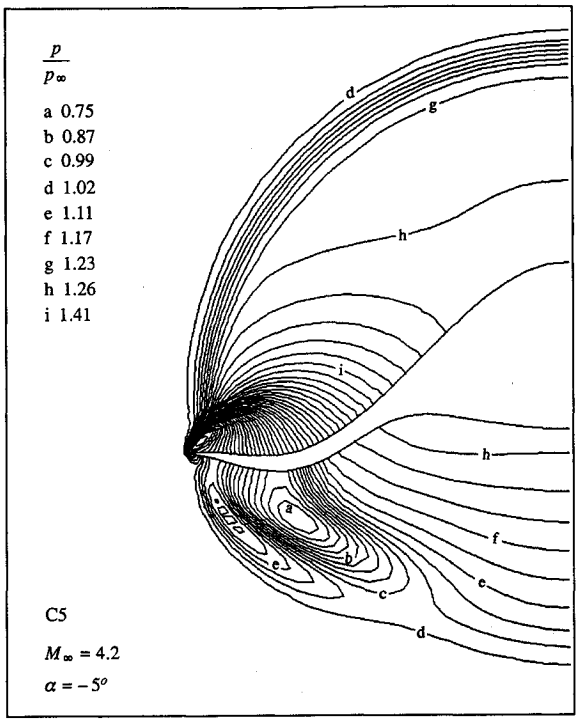

Fig. 13a Pressure contours in the base plane at Mach 4.2 and α = −5 deg for C5.

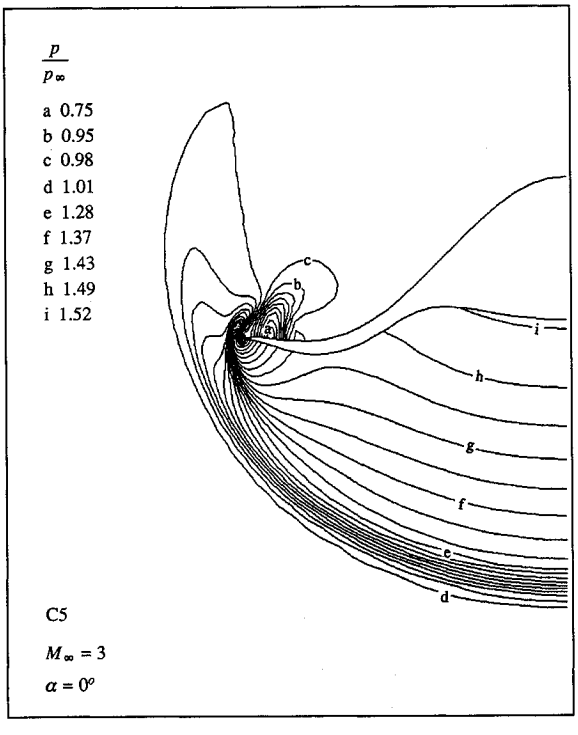

Fig. 13b Pressure contours in the base plane at Mach 3 and α = 0 for C5.

on C5 produces a stronger variation at the off-design Mach numbers.

Figure 15 shows the variation of L/D with α (for M_∞ = 4.2) for these configurations. For configurations C1, C2, and C3, the maximum L/D occurs at slight positive angle of attack, whereas the maximum L/D for configurations C4 and C5 occurs at a slight negative angle of attack. For all these configurations, C_L goes to zero at $\alpha = \alpha_{0L}$, for which we have approximately $\alpha_{0L} \approx -2\delta/5$,[18] but increases almost linearly for values of α greater than the zero lift value. Correspondingly, the drag coefficient C_D is a minimum at zero lift and

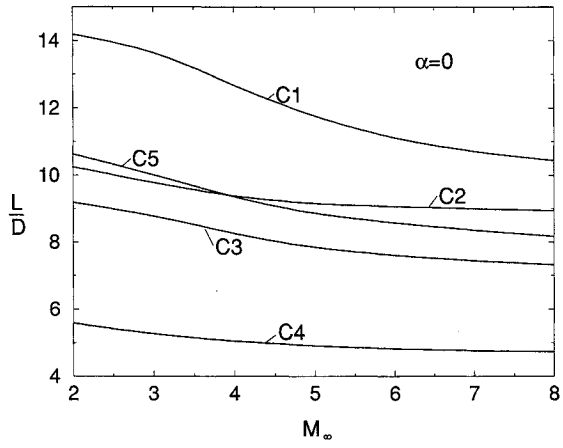

Fig. 14 L/D at off-design Mach numbers for Mach 4 waveriders.

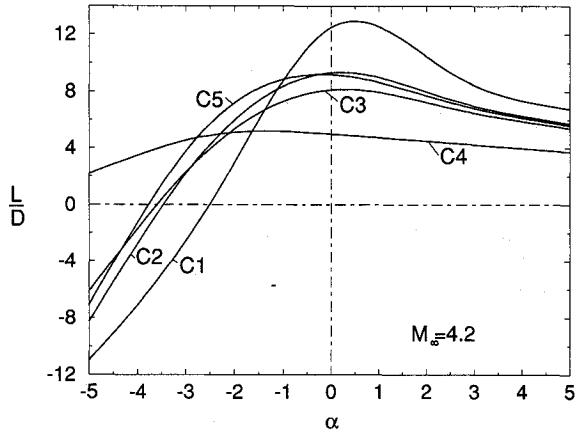

Fig. 15 L/D at angles of attack for Mach 4 waveriders.

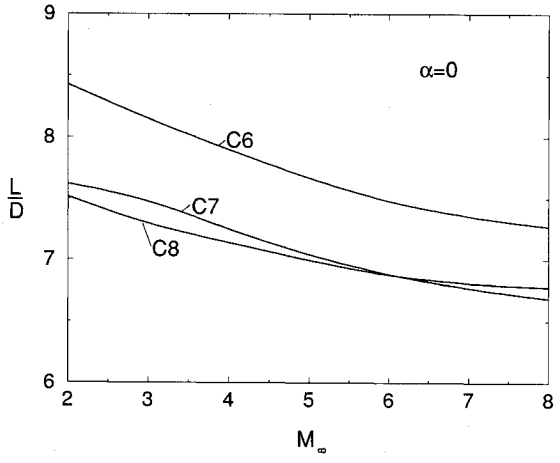

Fig. 16 L/D at off-design Mach numbers for Mach 8 waveriders.

increases nearly quadratically with $(\alpha - \alpha_{0L})^2$. As a condition of reference, it can be shown that L/D for a wedge is a maximum when α, measured relative to the upper surface, is slightly negative, i.e., when the upper surface is also a compression surface. As Fig. 15 shows, this is not true in general for arbitrary cone-derived waveriders.

Inviscid Results for M_∞ = 8

When the freestream Mach number becomes significantly larger than M_∞ = 4, at least two different kinds of effects become increasingly important. One is viscous-interaction effects and the other is heat transfer, especially near sharp leading edges. Some of the implications of viscous interaction have already been shown at M_∞ = 4. Here we will fasten our attention on the effects of rounding the sharp leading edges,

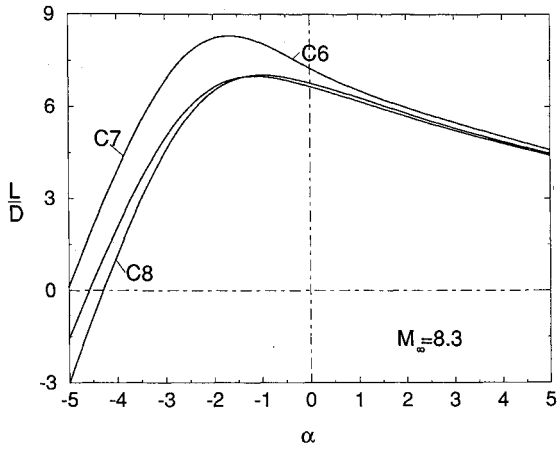

Fig. 17 *L/D* at angles of attack for Mach 8 waveriders.

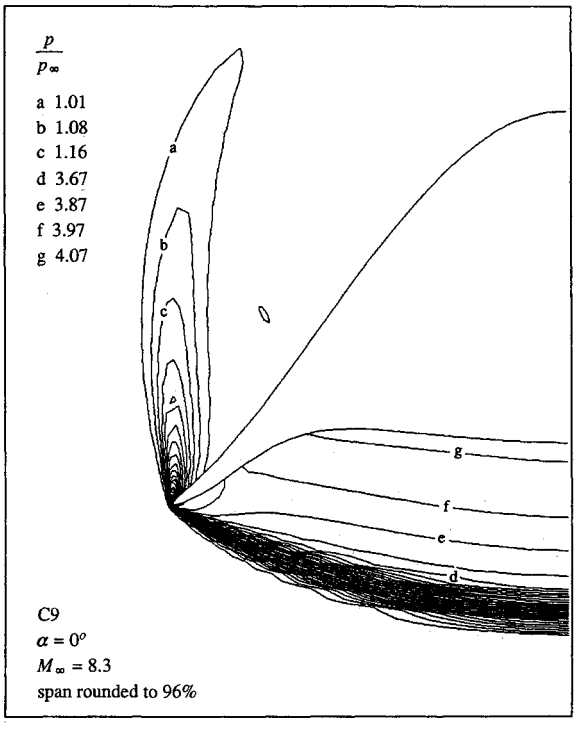

Fig. 18 Pressure contours at Mach 8.3 for C9 with span rounded to 96%.

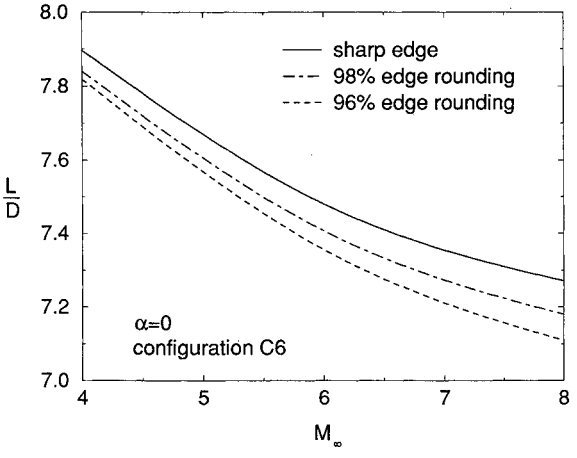

Fig. 19 Comparison of *L/D* for different rounding.

which is a means for reducing the large heat-transfer rates that occur there. For this purpose, we choose the waverider configurations labeled C6, C7, and C8 having the on-design Mach number $M_\infty = 8$. The configuration C6 has a trailing-edge tip thickness Λ_b that is a maximum for $M_\infty = 8$ and $\delta = 10$ deg, and it has a relatively large volume.[18,23] Configurations C7 and C8 are other relatively nonslender waveriders with somewhat different winglet shapes, having $\phi_l = 50$ deg instead of 27 deg for C6. Figure 16 shows the inviscid L/D vs M_∞ for $\alpha = 0$ for the lower off-design Mach numbers. The trends are similar, but configuration C6 has the overall larger L/D. Figure 17 shows L/D vs α for the on-design Mach number $M_\infty = 8.3$. The maximum L/D occurs at negative angles of attack, the more so for C6.

Figure 18 shows the pressure contours in the base plane with $M_\infty = 8.3$ and $\alpha = 0$ for configuration C6 with 96% rounding. For the sharp edge,[18] the disturbances are conical and are confined to the shock layer underneath the waverider. For the rounded edge, the shock stands off from the leading edge somewhat, and there are compression disturbances generated on the upper surface, the more so for greater rounding. The disturbances generated by the rounding are localized near the leading edge, and the inviscid flowfield around the remainder of the waverider is essentially unchanged.

Figure 19 shows L/D vs M_∞ for configuration C6 at $\alpha = 0$ for the different amounts of leading-edge rounding. For the greater rounding the loss in L/D is about 3% near the on-design Mach number $M_\infty = 8.3$, but it is less at the lower off-design Mach numbers since the shock tends to stand off from the leading edge there anyway. These results are typical for the other waveriders C7 and C8 also.

Conclusions

The off-design performance of a range of waverider shapes, on-design for $M_\infty = 4$ and $M_\infty = 8$, has been investigated by a space marching Euler code. For one of the configurations (C2), viscous results were obtained for $M_\infty = 4$ and $\alpha = 0$ by means of a time marching CFL3D code. Representative results are shown here, but further extensive calculations can be found in Ref. 18. Some of the pertinent observations are as follows:

1) For Mach numbers below the on-design values and at $\alpha = 0$, the leading-edge shock detaches and the inviscid L/D increases. For Mach numbers above the on-design values, the shock remains attached and the flow disturbances are confined to the shock layer beneath the waverider. Furthermore, L/D decreases, and a lambda-shock pattern tends to develop near the leading-edge region where extended winglets blend into the main body of the waverider.

2) When α is varied at the on-design Mach numbers, the maximum inviscid L/D occurs near $\alpha = 0$, but sometimes above and sometimes below depending on the configuration. Zero-lift and minimum wave drag occur approximately at $\alpha = -k\delta/2$, where k is a shape factor slightly less than unity. At large negative angles of attack, the shock is detached, and vortical regions appear near the leading edges on the undersides of the waveriders; this is especially pronounced for the waveriders with reflexed trailing edges.

3) The rounding of the leading edges produced disturbances that were localized near the leading edges. The value of L/D decreased slightly and was more pronounced near the on-design conditions.

4) At $M_\infty = 4$, the viscous interactions occurred near the leading edges, causing an effective standoff of the shock. The pressure increased near the leading edges on both the upper and lower surfaces, and was greater for the smaller Reynolds numbers. The results substantiated an HSDT analysis that incorporated laminar boundary-layer effects. Whereas the effects of viscous interaction were relatively small at $M_\infty = 4$, they can be expected to be substantially greater at larger Mach numbers, and such effects would be worthy of further study.

5) The results of the CFD calculations show the trends that can be expected for a wide range of waverider configurations at off-design conditions. They are consistent with the experimental results of Ref. 8. They also allow pictures of the flowfields to be portrayed that lend themselves to understanding the nature of the flowfields at the off-design conditions.

Acknowledgments

The authors gratefully acknowledge Ronald Cox for his advice on the numerical computations, and Lyle Long for arranging for the use of the IBM 3090 computer at Pennsylvania State University on which the Navier-Stokes calculations were made. The comments of G. Emanuel are also gratefully acknowledged. This work was partially supported by NASA Grant NAG-1-886.

References

[1]Nonweiler, T. R. F., "Delta Wings of Shape Amenable to Exact Shock Wave Theory," *Journal of Royal Aeronautical Society*, Vol. 67, No. 1, 1963, p. 39.

[2]Jones, J. G., "A Method for Designing Lifting Configurations for High Supersonic Speeds Using the Flow Fields of Nonlifting Cones," Royal Aircraft Establishment Rept. Aero 2624, A.R.C. 24846, UK, 1963.

[3]Rasmussen, M. L., "Waverider Configurations Derived from Inclined Circular and Elliptic Cones," *Journal of Spacecraft and Rockets*, Vol. 17, No. 6, 1980, pp. 537–545.

[4]Cole, J. D., and Zien, T. F., "A Class of Three-Dimensional Optimum Wings," *AIAA Journal*, Vol. 7, No. 2, 1969, pp. 264–271.

[5]Kim, B. S., Rasmussen, M. L., and Jischke, M. C., "Optimization of Waverider Configurations Generated from Axisymmetric Conical Flows," *Journal of Spacecraft and Rockets*, Vol. 20, No. 5, 1983, pp. 461–469.

[6]Bowcutt, K. G., Anderson, J. D., and Capriotti, D., "Viscous Optimized Hypersonic Waveriders," AIAA Paper 87-0272, Jan. 1987.

[7]Rasmussen, M. L., and He, X., "Analysis of Cone-Derived Waveriders by Hypersonic Small-Disturbance Theory," *Proceedings of the First International Hypersonic Waverider Symposium*, Dept. of Aerospace Engineering, Univ. of Maryland, College Park, MD, Oct. 1989, pp. 1–46.

[8]Rasmussen, M. L., Jischke, M. C., and Daniel, D. C., "Experimental Forces and Moments on Cone-Derived Waveriders for $M_\infty = 3$ to 5," *Journal of Spacecraft and Rockets*, Vol. 19, No. 6, 1982, pp. 592–598.

[9]Jischke, M. C., Rasmussen, M. L., and Daniel, D. C., "Experimental Surface Pressures on Cone-Derived Waveriders for $M_\infty = 3$ to 5," *Journal of Spacecraft and Rockets*, Vol. 20, No. 6, 1983, pp. 539–545.

[10]Jones, K. M., Talcott, N. A., and Shankar, V., "Application of a Full Potential Method for Computation of Three-Dimensional Supersonic Flows," AIAA Paper 84-0139, Jan. 1984.

[11]Jones, K. M., "Application of a Supersonic Full Potential Method for Predicting Supersonic Flowfields and Aerodynamic Characteristics," *Journal of Spacecraft and Rockets*, Vol. 23, No. 1, 1986, pp. 63–69.

[12]Jones, K. M., "Application of a Supersonic Full Potential Method for Analysis of Waverider Configurations," NASA TR 2608, Sept. 1986.

[13]Long, L. N., "Off-Design Performance of Hypersonic Waveriders," *Journal of Aircraft*, Vol. 27, No. 7, 1990, pp. 639–646.

[14]Liao, J. R., Isaac, K. M., and Miles, J. B., "Navier-Stokes Simulation for Cone-Derived Waverider," *AIAA Journal*, Vol. 30, No. 6, 1992, pp. 1521–1528.

[15]Yoon, B.-H., "Computational Analysis of Hypersonic Flows Past Elliptic-Cone Waveriders," Ph.D. Dissertation, Aerospace and Mechanical Engineering, Univ. of Oklahoma, Norman, OK, 1990.

[16]Jones, K. D., and Dougherty, F. C., "Computational Simulation of Flows about Hypersonic Geometries with Sharp Leading Edges," *Proceedings of the 8th Applied Aerodynamics Conference* (Portland, OR), AIAA, Washington, DC, 1990 (AIAA Paper 90-3065).

[17]Jones, K. D., Bauer, S. X. S., and Dougherty, F. C., "Hypersonic Waverider Analysis: A Comparison of Numerical and Experimental Results," AIAA Paper 91-1696, June 1991.

[18]He, X., "Computational Analysis of Hypersonic Flows Past Generalized Cone-Derived Waveriders," Ph.D. Dissertation, School of Aerospace and Mechanical Engineering, Univ. of Oklahoma, Norman, OK, 1992.

[19]Thomas, J. L., and Walters, R. W., "Upwind Relaxation Algorithms for the Navier-Stokes Equations," *AIAA Journal*, Vol. 25, No. 4, 1987, pp. 527–534.

[20]Lawrence, S. L., Tannehill, J. C., and Chaussee, D. S., "An Upwind Algorithm for the Parabolized Navier-Stokes Equations," AIAA Paper 86-1117, May 1986.

[21]Roe, P. L., "Approximate Riemann Solvers, Parameter Vectors and Difference Schemes," *Journal of Computational Physics*, Vol. 43, No. 2, 1981, pp. 357–372.

[22]Thompson, J. F., Thames, F. C., and Mastin, C. W., "Boundary-Fitted Curvilinear Coordinate Systems for Solution of Partial Differential Equations on Fields Containing Any Number of Arbitrary Two-Dimensional Bodies," NASA CR-2729, July 1977.

[23]He, X., and Emmanuel, G., "Nonslender Waveriders," *Journal of Aircraft*, Vol. 31, No. 1, 1994, pp. 125–131.